Article

Alkaline-Earth Metal Effects on Physical Properties of Ferromagnetic AVO$_3$ (A = Ba, Sr, Ca, and Mg): Density Functional Theory Insights

Md. Mijanur Rahaman,* Khandaker Monower Hossain, Mirza Humaun Kabir Rubel,*
A. K. M. Azharul Islam, and Seiji Kojima

Read Online

ACCESS		Metrics & More		Article Recommendations

ABSTRACT: The effects of alkaline-earth metals on electronic, optical, thermodynamic, and physical properties of ferromagnetic AVO$_3$ (A = Ba, Sr, Ca, and Mg) have been investigated by first-principles calculations within the GGA+U formalism based on density functional theory. The optimized structural parameters are in good agreement with the available experimental results that evaluate the reliability of our calculations. The cell and mechanical stability is discussed using the formation energy and Born stability criteria, respectively. The mechanical behaviors of AVO$_3$ are discussed on the basis of the results of elastic constants, elastic moduli, Peierls stress, and Vickers hardness. The nature of the ductile−brittle transition of AVO$_3$ compounds was confirmed by the values of Pugh's ratio, Poisson's ratio, and Cauchy pressure. The electronic band structures, as well as density of states, reveal the half-metallic behavior of BaVO$_3$ and SrVO$_3$. However, CaVO$_3$ and MgVO$_3$ exhibit spin-gapless and magnetic semiconductor characteristics, respectively. The microscopic origin of the transition from the half-metallic to semiconductor nature of AVO$_3$ is rationalized using electronic properties. The presence of covalent, ionic, and metallic bonds in AVO$_3$ compounds is found by the analysis of bonding properties. The single-band nature of half-metallic AVO$_3$ is seen by observing hole-like Fermi surfaces in this study. Furthermore, the various thermodynamic and optical properties are calculated and analyzed. The refractive index suggests that AVO$_3$ could be a potential candidate for applications to high-density optical data storage devices.
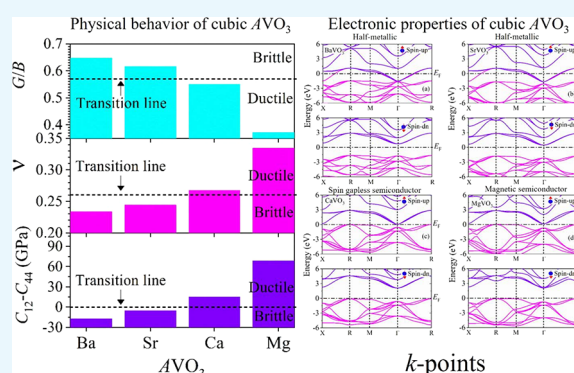
1. INTRODUCTION

The understanding of ABO$_3$-type oxide perovskites is crucial not only due to their structures and properties being modified by the exchange of distinct elements into their crystallographic equivalent sites but also for investigating phase transitions. This type of material is also fundamentally interesting and bears technological importance because of its ferroelectric, multiferroic, magnetic, and superconducting properties,[1−5] which originate from an interplay between the chemical composition and the structure type. Recently, the study of AVO$_3$ (A = Ba, Sr, Ca, and Mg) has been given much attention because of the strong couplings between the lattice degrees of freedom and spin,[6−8] which makes them a potential candidate for the application to spintronics devices. It has been found that few atoms at the A site in AVO$_3$, e.g., PbVO$_3$, showed antiferromagnetic ordering with large spontaneous polarization.[9,10] Belik *et al.* also reported the insulator to metal transformation, induced by crystal symmetry variations from the tetragonal to cubic phase in PbVO$_3$.[11]

AVO$_3$ (A = Ba, Sr, Ca, and Mg) have been synthesized by using high-temperature and high-pressure (HTHP) conditions for investigating their structural and relevant properties.[12−15]

BaVO$_3$ showed a polycrystalline phase with a cubic perovskite structure under high pressures, and it should be noted that Ba$_3$(VO$_4$)$_2$ was formed instead of BaVO$_3$ when either the pressure or temperature was insufficient.[12] Notably, SrVO$_3$ and CaVO$_3$ have correlated Mott conductors in which SrVO$_3$ is cubic perovskite, and their oxygen nonstoichiometric effects on the structures and electronic states are investigated extensively.[13,14,16,17] Strontium vanadate has a simple cubic perovskite structure with a = 3.842 Å that exhibits Pauli paramagnetic and metallic characteristics near room temperature as well.[16] Additionally, the dielectric function, the band structure, the Fermi surface, and interband optical transitions of the SrVO$_3$ transparent conducting thin film have also been analyzed from the first-principles study.[16] Moreover, this material has attracted great attention as a potential oxide

electrical conductor.[18,19] However, stoichiometric CaVO$_3$ belongs to the orthorhombic phase, while nonstoichiometric CaVO$_{3-\delta}$ (0.04 < δ < 0.08) and CaVO$_{3-\delta}$ (δ = 0.20) show cubic and monoclinic phases, respectively.[14,20] In addition, the slightly oxidized CaVO$_{3.05}$ exhibits insulating behavior without any significant structural changes.[21] At ambient pressure, Chamberland *et al.* reported the orthorhombic crystal structure of MgVO$_3$, whereas the high-pressure adjustment of MgVO$_3$ exhibited a triclinic structure.[22] The electronic band structure with various spin arrangements for MgVO$_3$ showed paramagnetic as well as magnetic solutions with ferro- and antiferromagnetic ordering.[23] Between them, the paramagnetic solution has metallic behavior, whereas the band splits into two in the magnetic solutions with an insulator gap in ferro- and antiferromagnetic states.[23] Hence, with the substitution of distinct A site cations, a perovskite may show various stable phases and correspondingly diverse material peculiarities. Therefore, it is interesting to discover the electronic, optical, and diverse physical properties of AVO$_3$ perovskites, where A is a divalent cation.

Nowadays, the cubic phase of oxide perovskite materials is an extensive research area for the proper explanation of electronic, elastic, vibrational, thermodynamic, and optical properties for emergent applications. Recently, Kamruzzaman *et al.*[24] reported a comparative study on the cubic phases of ATiO$_3$ (A = Ba, Ca, Pb, and Sr) by first-principles calculations. The first-principles calculations on the cubic phase of simple and double-perovskite Bi oxide magnetic materials, which exhibited superconductivity, envisage different interesting physical properties including electronic, mechanical, and thermodynamic properties as well.[3,25,26] The cubic perovskite structures of AVO$_3$ (A = Ba, Sr, Ca, and Mg) are our point of interest in the present investigation. The cubic phase with $Pm\bar{3}m$ symmetry of SrVO$_3$ and BaVO$_3$ was reported experimentally,[12,13] whereas CaVO$_3$ and MgVO$_3$ show an intrinsically orthorhombic phase.[14,15] The cubic phase of CaVO$_3$ and MgVO$_3$ may be comprehended by using specifically designed growth conditions similar to those implemented for achieving hexagonal Si.[27] Rashid *et al.*[28] reported metallic behavior in both spin channels of cubic BaVO$_3$ and LaVO$_3$ using the GGA-PBE exchange−correlation, while the utilization of the mBJ scheme explicated a clear half-metallic ferromagnetic behavior. They discussed the electronic and thermoelectric properties of BaVO$_3$ and LaVO$_3$. The electronic, magnetic, and optical properties in the low-energy range (0−15 eV) of cubic AVO$_3$ (Ba, Sr, and Ca) were studied by first-principles calculations.[29] However, extensive studies on the alkaline-earth metal's effects on physical properties (elastic constants, elastic moduli, Peierls stress, Pugh's and Poisson's ratio, Cauchy pressure, and Vickers hardness), the Fermi surface, electronic charge density, and population analysis are rather scarce, which are crucial for accelerating the applications and understanding of these material systems precisely.

In this study, we have investigated the structural, physical (elastic constants, Young's, shear, and bulk moduli, Pugh's and Poisson's ratio, Cauchy pressure, Peierls stress, and Vickers hardness), electronic (the band structure, charge density map, DOS, and Fermi surface), optical (the dielectric function, photoconductivity, refractive index, reflectance, and absorbance), population analysis, and thermodynamic properties (melting temperature, Debye temperature, and minimum thermal conductivity) considering the cubic phase of ferromagnetic AVO$_3$ by altering cations Ba, Sr, Ca, and Mg

employing density functional theory (DFT)-based CASTEP code. The possibility of applications to high-density optical data storage devices of AVO$_3$ has been discussed on the basis of observed optical properties.

2. COMPUTATIONAL METHODS

The present calculations based on density functional theory (DFT)[30,31] were carried out with the Cambridge Serial Total Energy Package (CASTEP) code[32] utilizing the GGA+U parameterization scheme. The spin-polarized scheme using formal spin as the initial state with charge neutrality conditions was implemented in the relatively high-level computation GGA+U method. The default value of Hubbard U = 2.5 eV for V 3d was set for computations in this study. The ultrasoft pseudopotential formalism of the Vanderbilt type[33] was utilized for all atoms to simulate the interactions of valence electrons with ion cores. The choice of exchange−correlation functionals (XCs) was regarded as a crucial parameter for first-principles calculations. Therefore, geometry optimization of the cubic structure of BaVO$_3$ with $Pm\bar{3}m$ symmetry with fully relaxed structures was performed by the Broyden−Fletcher−Goldfarb−Shannon (BFGS) algorithm[34] using various XCs to search the ground state to obtain the best lattice parameters and compare them with the available experimental ones. The XC that induced the best results for BaVO$_3$ was used to calculate all properties of AVO$_3$ (A = Ba, Sr, Ca, and Mg) by altering the A cations. The electronic wave function with a cutoff energy of 700 eV was used for all calculations of cubic AVO$_3$ with a ferromagnetic (FM) configuration because the FM state was relatively more stable than the antiferromagnetic (AFM) state.[29] According to the Monkhorst−Pack scheme,[35] 12 × 12 × 12 k-point grids were employed for sampling the irreducible Brillouin zone. In the present calculations, the convergence tolerances for geometry optimization were set to be 1 × 10^{-6} eV/atom (total energy), 0.03 eV/Å (maximum force on atoms), 0.001 Å (maximum atom displacements), and 0.05 GPa (maximum stress).

3. RESULTS AND DISCUSSION

3.1. Structural Parameters and Cell Stability. The oxide perovskites AVO$_3$ (A = Ba and Sr) belong to the cubic phase with $Pm\bar{3}m$ (no. 221) symmetry consisting of an A atom at the corner, V in the body center, and O at the face center of the cube.[12,13] The cubic phase of nonstoichiometric CaVO$_{3-\delta}$ (0.04 < δ < 0.08) was reported experimentally by Ueda,[14] while stoichiometric CaVO$_3$ and MgVO$_3$ showed an orthorhombic phase.[14,15] To realize the cubic phase of CaVO$_3$ and MgVO$_3$, specifically designed growth schemes similar to those implemented for observing hexagonal Si are necessary.[27] First, the crystal structure of BaVO$_3$ was sketched using the available refinement data[12] in this study. After that, the structures were absolutely relaxed with the lattice parameters and internal coordinates in order to optimize the geometry by swapping A site cations. The crystal structures of the cubic AVO$_3$ (A = Ba, Sr, Ca, and Mg) system are depicted in Figure 1. The optimized lattice parameters of AVO$_3$ substances, both theoretical and experimental data, are summarized in Table 1. The calculated values of lattice parameters match reasonably with the experimental results,[12−14] and the relation is noted as follows: a(BaVO$_3$) > a(SrVO$_3$) > a(CaVO$_3$) > a(MgVO$_3$). The resultant interatomic distance decreases with decreasing atomic radii
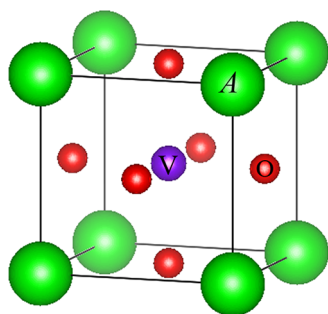
Figure 1. (Color online) Unit cell of cubic perovskite AVO_3 (A = Ba, Sr, Ca, and Mg).

from the bottom to top in a group, which results in a decreasing trend in lattice parameters. Interestingly, these consequences are similar to those observed in $ATiO_3$ (A = Ba, Ca, Pb, and Sr) compounds.[24] Moreover, the chemical stability of AVO_3 can be confirmed by analyzing their formation energies. The formation energy (ΔE_f) is approximated by the subtraction of the total energies of pure constituent atoms from the total energy of the materials in their stable structures. The magnitude of ΔE_f of AVO_3 is estimated by the following expression:[36]

$$\Delta E_f(AVO_3) = [E_{tot}(AVO_3)_{fu} - E_s(A) - E_s(V) - 3E_s(O)] \tag{1}$$

Here, $E_{tot}(AVO_3)_{fu}$ represents the total energy per formula unit and is given by $E_{tot}(AVO_3)_{fu} = 1/N[E_{tot}(AVO_3)_{cell}]$, where N denotes the number of formula units per unit cell. $E_s(A)$, $E_s(V)$, and $E_s(O)$ are the total energies per atom of the pure elements A, V, and O, respectively, in their ground-state solid phases. So, ΔE_f per atom $= \Delta E_f(AVO_3)_{fu}/N_t$, where N_t denotes the total number of atoms in one formula unit. The calculated formation energies of ferromagnetic AVO_3 are also displayed in Table 2. It is seen from Table 2 that the energies of AVO_3 are negative, indicating that the compounds are energetically stable.

3.2. Physical Properties. *3.2.1. Elastic Moduli and Peierls Stress.* The study of numerous physical characteristics such as elastic anisotropy, both brittle and ductile nature, and elastic moduli is crucial for industrial applications of engineering materials. The elastic constants C_{ij} are obtained from the linear finite stress−strain approach within the CASTEP code.[37] The calculated three independent elastic constants, namely, C_{11}, C_{12}, and C_{44}, for cubic AVO_3 are displayed in Table 2. The mechanical stability of a lattice can be determined by Born stability criteria that are commonly formulated in terms of C_{ij} and hence based on free energy considerations.[38] For a cubic crystal, the mechanical stability criteria are $C_{11} + 2C_{12} > 0$, $C_{11} - C_{12} > 0$, and $C_{44} > 0$, which stand for spinodal, shear, and Born criteria, respectively. The spinodal criterion is equivalent to insisting on a positive bulk modulus, B. Hence, the mechanical stability of a cubic crystal requires that the elastic

Table 2. The Calculated Lattice Constant, a, Volume, V, and Formation Energy ΔE_f of AVO_3 Compounds Together with Available Experimental Results

compounds	a (Å)	V (Å^3)	ΔE_f (eV/atom)	refs.
$BaVO_3$	3.927	60.547	−7.601	present calc.
	3.943(3)			12
$SrVO_3$	3.830	56.185	−7.626	present calc.
	3.843(1)			13
$CaVO_3$	3.774	53.752	−7.635	present calc.
$CaVO_{3−\delta}$	3.786(3)			14
$MgVO_3$	3.741	52.358	−6.986	present calc.

constants B, $C_{11} - C_{12}$, and C_{44} be positive. Following these stability conditions, the calculated elastic constants are presented in Table 2. Therefore, the chosen cubic phase of AVO_3 in this investigation is mechanically stable. The tendency of a solid to deform non-permanently in diverse directions with applied stress is measured by its elastic property. The elastic constants provide information about the bonding behavior of solids as well. The elastic constant C_{11} gives the elasticity along the axial length. So, the elastic stiffness of solids against the $\langle 100 \rangle$ uniaxial strain of the (100) plane can be signified by the value of C_{11}. The elasticity in shape is given by the elastic constants C_{12} and C_{44}, where C_{44} denotes the shear stress in the (010) plane along the $\langle 001 \rangle$ direction and C_{12} indicates the pure shear stress in the (110) plane in the $\langle 110 \rangle$ direction. As can be seen in Table 3, $CaVO_3$ has the largest value of C_{11} compared to others. It is worth noting that the calculated value of C_{11} for all perovskites is higher than C_{12}, indicating that the bonding strength along the $\langle 100 \rangle$ direction is higher than that along the $\langle 110 \rangle$ directions in AVO_3. This result indicates that the elasticity in length is stiffer than the elasticity in shape. The Kleinman parameter (ξ) measures the ease of bond bending to bond stretching. In general, the value of ξ can be between 0 and 1 ($0 \leq \xi \leq 1$) and is estimated using the following expression:[39]

$$\xi = \frac{C_{11} + 8C_{12}}{7C_{11} + 2C_{12}} \tag{2}$$

Kleinman reported that the upper limit corresponds to a minimized bond bending term and the lower limit corresponds to a minimized bond stretching term.[40] The calculated value of ξ for AVO_3 compounds is shown in Table 2. The estimated value of ξ of ∼0.50 for AVO_3 compounds is in good agreement with the previously reported value of ξ of ∼0.555 for perovskite $LaAlO_3$.[41] The calculated value of ξ suggests the strong bonding nature of AVO_3, which is dominated by the bond bending compared to the bond stretching.

The various elastic properties such as the bulk modulus, B, shear modulus, G, Young's modulus, E, and Poisson's ratio, ν, are calculated from the single-crystal zero-pressure elastic constants using well-known relationships.[42,43] The calculated elastic parameters are shown in Table 2. The constituent

Table 1. The Optimized Lattice Parameter, a (Å), of $BaVO_3$ with Different XCs and Compared with the Available Experimental Results

|	exchange−correlation functions (XCs)					
	PBE	RPBE	PW91	WC	PBEsol	expt[a]
lattice parameter	3.97846	4.01721	3.97463	3.92674	3.92391	3.94288

[a]Ref 12.

Table 3. The Elastic Constants, C_{ij} (GPa), Bulk Moduli, B (GPa), Shear Moduli, G (GPa), Young's Moduli, E (GPa), the Kleinman Parameter, ξ, the Burgers Vector, b (Å), the Interlayer Distance, d (Å), and Peierls Stress, σ_p (GPa), of AVO₃ Compounds

compounds	C_{11}	C_{12}	C_{44}	B	G	E	ξ	b	d	σ_p	H_V
BaVO₃	300	116	134	177	115	283	0.527	3.927	1.963	2.489	16.4
SrVO₃	335	113	118	187	115	287	0.482	3.830	1.915	2.380	15.2
CaVO₃	351	113	98	192	106	268	0.468	3.774	1.887	1.985	12.3
MgVO₃	345	124	56	198	74	197	0.502	3.741	1.871	0.990	4.9

atom's average bond strength for a given solid is assessed by the bulk modulus.[44] Recently, Rahaman *et al.* found the moderate bonding strength in LiCuBiO₄ by observing the bulk modulus of 101 GPa.[47] However, Nasir *et al.* reported the strong bonding in ScIrP and ScRhP by the bulk moduli of 190 and 171 GPa, respectively.[45] Thus, the calculated values of B in the range of 177−198 GPa (Table 2) may imply the strong bonding strength of atoms involved in AVO₃. It is also seen from Table 2 that the bulk modulus improves by varying cations from Ba to Mg. The cationic size decreases the compressibility of the compounds, making the solid dense that enhances the bulk modulus of AVO₃. The bond strength of atoms also gives the required resistance to volume deformation under external pressure. In contrast, the G evaluates the change of shape in a solid, which exhibits a crucial relationship with the hardness of materials. The material becomes more rigid when the value of G becomes greater. The Young's modulus, E, exerts an influence on the thermal shock resistance of solid matter. The critical thermal shock coefficient varies inversely with respect to E.[46] The greater the value of the thermal shock coefficient, the better the thermal shock resistance. A material is chosen as a thermal barrier coating (TBC) substance based on thermal shock resistance. Notably, AVO₃ has a comparatively higher Young's modulus, and hence, it might not be suitable as a TBC material. However, the calculated value of E (197−287 GPa) indicates that AVO₃ is moderately stiff.[47] The moduli of elasticity such as G, B, and E are not only useful to explain the mechanical properties of solids but also effective to estimate the hardness of materials. C_{44} is the best one to predict the hardness of solids among the observed elastic constants. Moreover, the shear modulus (G) is considered as the best hardness predictor among the moduli of elasticity as well. It is evident from Table 3 that BaVO₃ is harder than the rest of the compounds in this study. These statements may be strengthened by the calculations of hardness by Chen's formula,[48] which can be expressed as $H_V = 2(k^2 G)^{0.585} - 3$, where k is the Pugh ratio (G/B). The estimated values of H_V are displayed in Table 3 and found to be consistent with the earlier predictions based on the values of C_{44} and G. Mazhnik and Oganov[49] reveal conducive agreement between the experimental and theoretical values of hardness of different materials calculated using Chen's formula. It is well-established that diamond (H_V = 96 GPa), BC₂N (H_V = 76 GPa), and BC₅ (H_V = 71 GPa) are widely used as superhard materials.[49] Thus, the much lower harness of AVO₃ in comparison with superhard materials confirms that the studied compounds do not belong to superhard materials. However, the value of H_V of half-metallic BaVO₃, SrVO₃, and CaVO₃ is comparable with hard refractory materials NbC (H_V = 16.0 GPa), GaN (H_V = 15.1 GPa), and GaN (H_V = 12.0 GPa), respectively, whereas the H_V value of MgVO₃ is comparable with the semiconductor AlAs (H_V = 5.0 GPa).[49] The relatively large value of hardness denotes that BaVO₃, SrVO₃, and CaVO₃ are not machinable,

whereas MgVO₃ is machinable by conventional cutting machines.

Furthermore, the study of failure modes, i.e., the ductile or brittle nature of a material, is technologically very important. For most practical situations, a material may be classified as either brittle or ductile. Figure 2 shows the graphical
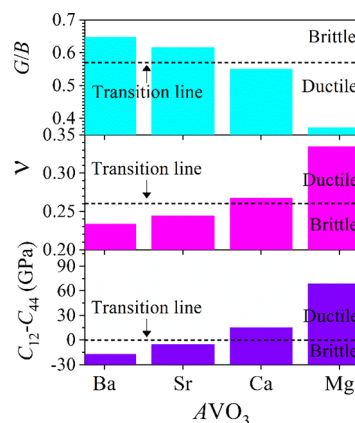
Figure 2. (Color online) Calculated Pugh's ratio (G/B), Poisson's ratio (ν), and Cauchy pressure ($C_{12}-C_{44}$) showing the graphical representation of ductile/brittle behavior of AVO₃ (A = Ba, Sr, Ca, and Mg). The horizontal dashed lines indicate the ductile−brittle transition line.

representation of ductile materials from brittle materials for all considered perovskite materials. If the value of Pugh's ratio (G/B) is higher than 0.57, then the material is said to be brittle;[50] otherwise, it is ductile. It is apparent from the upper part of Figure 2a that BaVO₃ and SrVO₃ are brittle materials, whereas the nature of CaVO₃ is at around the ductile−brittle transition line; on the other hand, MgVO₃ exhibits a ductile nature. In addition to Pugh's ratio, Frantsevich *et al.* also proposed a critical value of Poisson's ratio (ν of ∼0.26) for separating the brittle and ductile nature of solids.[51] The calculated values of ν (middle part of Figure 2a) again confirm that BaVO₃ and SrVO₃ are purely brittle, while MgVO₃ is a completely ductile material. However, CaVO₃ is the crossover of the brittle to ductile transition. The Cauchy pressure, defined as $C_{12}-C_{44}$, is another indicator of failure mode of materials.[52] If the Cauchy pressure is negative, then the material is expected to be brittle; otherwise (having a positive Cauchy pressure), it is a ductile one.[52] Hence, in this study, BaVO₃ and SrVO₃ are assumed to be brittle, whereas CaVO₃ and MgVO₃ are ductile in accordance with the aforementioned three indicators.

The Peierls stress represented by σ_p is the force required to move a dislocation inside an atomic plane in the unit cell, which measures the strength of a crystal through displacing dislocations. Therefore, Peierls stress can provide the knowl-

edge to accelerate dislocation in a glide plane of the synthesized cubic perovskite crystals as well. The Peierls stress can be estimated using the shear modulus (G) and the Poisson ratio (ν) as follows:[53]

$$\sigma_p = \frac{G}{1-\nu} \exp\left[-\frac{2\pi d}{b(1-\nu)}\right] \qquad (3)$$

Herein, d and b denote the interlayer distance between the glide planes and the Burgers vector, respectively. The calculated interlayer distance (d), the Burgers vector (b), and the resulting Peierls stress (σ_p) of AVO_3 are presented in Table 3. It is seen from Table 3 that the values of σ_p decrease as we follow the sequence Ba→Sr→Ca→Mg. The lowest and highest values of estimated Peierls stress are 0.990 and 2.489 GPa for $MgVO_3$ and $BaVO_3$, respectively. The σ_p values of $BaVO_3$, $SrVO_3$, and $CaVO_3$ are comparable to the reported double cubic perovskite $(Na_{0.25}K_{0.45})Ba_3Bi_4O_{12}$,[54] whereas the σ_p value of $MgVO_3$ is comparable to the reported simple cubic perovskite $(Ba_{0.62}K_{0.38})(Bi_{0.92}Mg_{0.08})_4O_{12}$.[24] The calculated values of σ_p for AVO_3 compounds can also be compared with several inverse perovskites Sc_3InX (X = B, C, and N) with σ_p values ranging from 3.06 to 5.31 GPa[55] and those of MAX phases Y_2AlC (Y = Nb, Ta, V, Cr, and Ti) ranging from 0.74 to 0.98 GPa.[56] Furthermore, the reported σ_p values for rocksalt binary carbides TiC, VC, and CrC are between 17.46 and 22.87 GPa.[56] The value of σ_p of AVO_3 exhibits the sequence σ_p (MAX phases) < σ_p (AVO_3 perovskites) < σ_p (selected inverse perovskites) ≪ σ_p (binary carbides). Hence, it is apparent that dislocations can move easily in the selected MAX phases, but the movement of dislocation is almost impossible in the case of the binary carbides. Since AVO_3 (A = Ba, Sr, and Ca) perovskites in the present study show an intermediate value of σ_p larger than the MAX phases but smaller than the selected inverse perovskites, so, the dislocation movement may still be observed here but not as easily as in MAX phases. The value of σ_p for $MgVO_3$ is similar to that of the MAX phase Ti_2AlC[56] and smaller than those of $BaVO_3$, $SrVO_3$, and $CaVO_3$. So, the movement of dislocation in $MgVO_3$ may occur more easily than in other perovskites and the same as in the MAX phase Ti_2AlC under this study.

3.2.2. Elastic Anisotropy. Elastic anisotropy influences various types of physical processes, such as microscale cracking in ceramics, development of plastic deformation in crystals, mechanical yield points, enhanced charged defect mobility, internal friction, and elastic instability. In a cubic phase, Zener's anisotropy index $[A_G = 2C_{44}/(C_{11} - C_{12})]$ is one of the important parameters to determine whether the crystal is isotopic or not. The material will be isotropic only if A_G becomes unity. The deviation of A_G from unity measures the degree of elastic anisotropy, and more deviation means more anisotropy. Another important measure of anisotropy, namely, the universal anisotropy index A^U, is defined as $A^U = 5\frac{G_V}{G_R} + \frac{B_V}{B_R} - 6 \geq 0$, where the subscripts denote the upper bound (Voigt, V) and the lower bound (Reuss, R) of B and G. Here, $A^U = 0$ indicates the isotropic nature of materials, and the deviation from zero characterizes the elastic anisotropy of crystals. It is apparent from Figure 3b that the values of A_G and A^U of $SrVO_3$ are close to the isotropic line, whereas values of A_G and A^U significantly deviate from the isotropic line in the cases of $BaVO_3$, $CaVO_3$, and $MgVO_3$. These results indicate
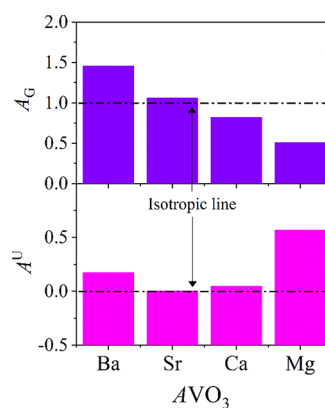

Figure 3. (Color online) Isotropic/anisotropic nature of AVO_3 shown graphically by Zener's anisotropy index (A_G) and the universal (A^U) anisotropy index, where the dash-dotted lines denote the isotropic line.

that $BaVO_3$, $CaVO_3$, and $MgVO_3$ are anisotropic, but $SrVO_3$ represents very weak or reasonably negligible anisotropy.

The three-dimensional (3D) dependences of the shear modulus, G, Young's modulus, E, and Poisson's ratio, ν, of AVO_3 are studied in order to depict the elastic anisotropy visually as well as quantitatively. The 3D directional dependence of G, E, and ν is depicted in Figure 4. The 3D surface should exhibit a spherical shape for a perfectly isotropic compound. It is seen in Figure 4 that the 3D surface of G, E, and ν of $SrVO_3$ has an almost spherical shape. This result clearly indicates that $BaVO_3$, $SrVO_3$, and $MgVO_3$ are anisotropic compounds, whereas $SrVO_3$ is a compound with weak or negligible anisotropy. The minimum and maximum values of G, E, and ν of the materials are shown in Table 4 for comparison among the four compounds. The 3D plots as well as numerical values of different anisotropy indices reveal that $MgVO_3$ is the most prominent anisotropic compound among the four compounds, and the relation $MgVO_3$ > $BaVO_3$ > $CaVO_3$ > $SrVO_3$ was observed.

3.3. Electronic Properties. *3.3.1. Electronic Band Structures.* The calculated electronic band structures of AVO_3 with a ferromagnetic configuration are depicted in Figure 5, where the horizontal dash-dotted lines denote the Fermi level, E_F. The splitting of energy in the spin-polarized electronic band structure is clearly seen, which appears owing to the existence of vanadium cations in the studied perovskites. It is seen from Figure 5 that the valence and conduction bands of $BaVO_3$ and $SrVO_3$ appreciably overlap with each other and cross the Fermi level in the spin-up channel (Figure 5a,b), resulting in no band gap at the E_F, indicating that the free carriers are available to show metallic conductivity, while the spin-down (spin-dn) channel exhibits an indirect band gap (R−Γ) semiconductor-like behavior because the Fermi level lies inside the forbidden gap. However, the valence band of $CaVO_3$ and $MgVO_3$ touches the Fermi level in both spin-up and spin-down channels as shown in Figure 5c,d, while the conduction band of $CaVO_3$ touches the Fermi level in the spin-up channel, but a clear energy gap is found for the spin-down channel. In contrast, there is a tiny (E_g of ∼0.12 eV) and wide energy gap (E_g of ∼2.19 eV) between the conduction band and the Fermi level in spin-up and spin-down channels for MgO_3, respectively. For the spin-up state of $CaVO_3$, no overlapping and also a negligible energy gap (E_g of ∼0.03 eV) between the valence and conduction bands are observed (Figure 5c); this
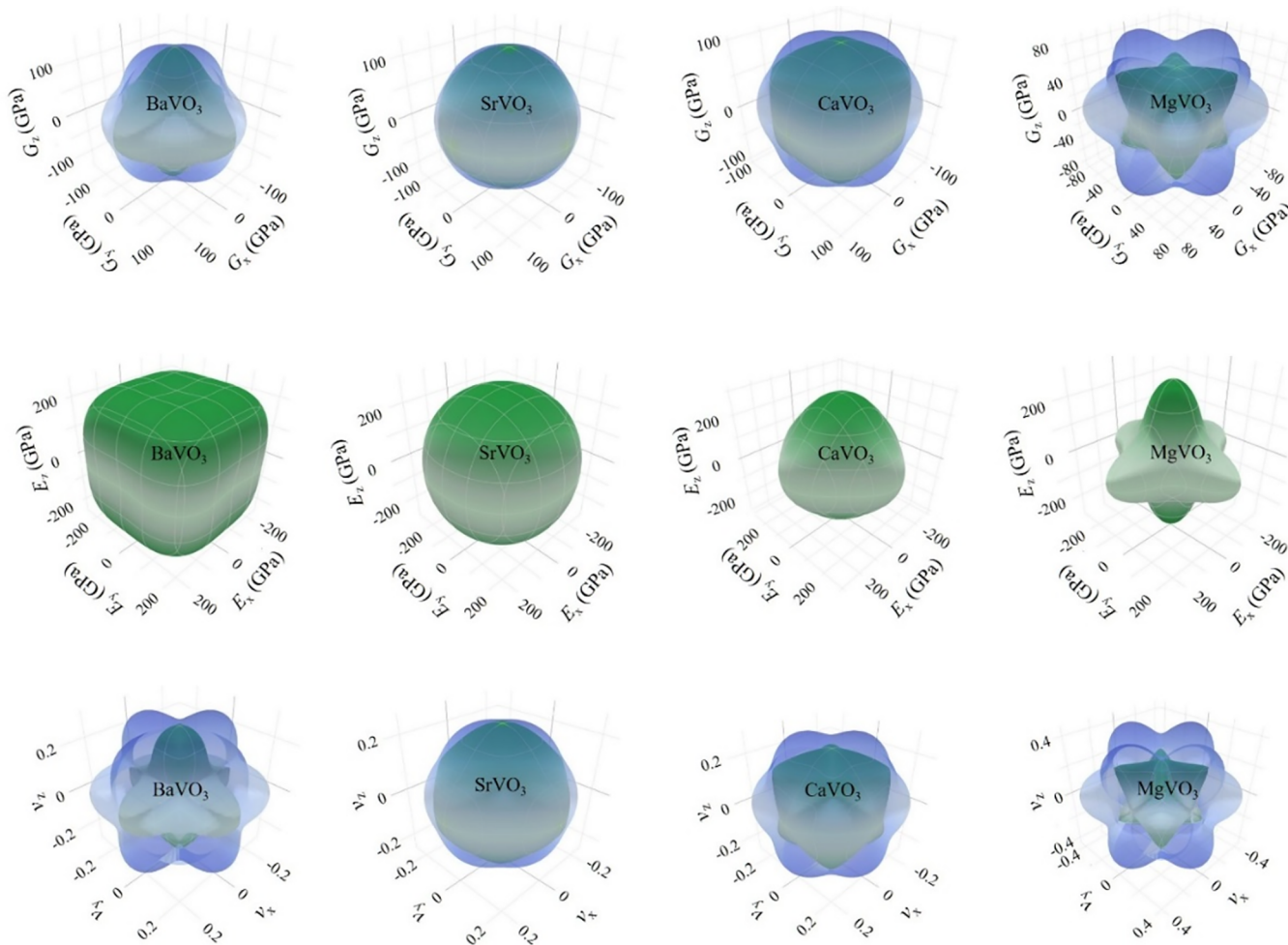
Figure 4. (Color online) Directional dependences of the shear modulus, G (upper curves), Young's modulus, E (middle curves), and Poisson's ratio, ν (lower curves), of AVO$_3$ (A = Ba, Sr, Ca, and Mg).

Table 4. The Maximum and Minimum Limits of G, Y, and ν of AVO$_3$ (A = Ba, Sr, Ca, and Mg)

compounds	shear modulus (GPa)		Young's modulus (GPa)		Poisson's ratio	
	G_{max}	G_{min}	E_{max}	E_{min}	ν_{max}	ν_{min}
BaVO$_3$	133.62	91.59	320.41	234.41	0.350	0.098
SrVO$_3$	118.07	110.93	292.60	277.83	0.262	0.223
CaVO$_3$	118.94	97.68	295.80	250.58	0.334	0.214
MgVO$_3$	110.13	56.00	278.68	153.52	0.544	0.165

finding suggests the spin-gapless semiconductor behavior of CaVO$_3$. Hence, the overall behavior of BaVO$_3$ and SrVO$_3$ is half-metallic ferromagnetic, whereas ferromagnetic CaVO$_3$ and MgVO$_3$ behave like spin-gapless and magnetic semiconductors, respectively. It is significant that the valence band of CaVO$_3$ and MgVO$_3$ is very flat just below the E_F with a large dispersion from the R to M point, which may create a van Hove singularity (vHS) at both points. The presence of such a vHS in the band diagram usually denotes the enhanced electronic and electrical carriers as well as electron pairings in the case of superconducting materials.[3,57] Hence, the presence of a flat band might be the possible reason for the spin-gapless and magnetic semiconductor nature of CaVO$_3$ and MgVO$_3$, respectively. Mahmood et al.[29] reported the half-metallic ferromagnetic behavior of AVO$_3$ (A = Ba, Sr, and Ca) as

well. The electronic properties of AVO$_3$ (A = Sr, Ba, and Pb) also revealed the half-metallic nature studied by Yan et al.[58] The band gap of ferromagnetic MgVO$_3$ was also reported at about 0.5 eV within the local spin density approximation (LSDA).[22] In this study, the half-metallic nature of AVO$_3$ (A = Ba, Sr, and Ca) is 100% spin-polarized because all the states are present in the spin-up channel, while the spin-down channel has no states. The indirect band of the studied AVO$_3$ compounds may arise owing to the exchange splitting.[29] It is significant that the indirect band gap in the spin-down channel decreases with the cation changing from Ba to Ca as shown in Figure 7. The results are similar to those observed in ref 29.

3.3.2. Density of States (DOS). In order to have a better understanding, the atomic contributions to the band formation of AVO$_3$ compounds, the partial density of states (PDOS), and the total density of states (DOS) have been calculated and are plotted in Figure 6. It is evident from DOS that all the compounds have n-type carriers[59] with a sharp peak for the crossing of electrons at E_F. Among them, MgVO$_3$ has a relatively lower class of carriers because of its semiconducting nature. The lower band of AVO$_3$ for both spin-up and spin-down channels is situated at about −65 eV, which originated from V 4s states, whereas the lowest band of MgVO$_3$ is located at around −75 eV, which stemmed from the Mg 3s state only. The band of BaVO$_3$ originated from the V 3p state for both channels and is situated at around −39 eV and shifts to a little
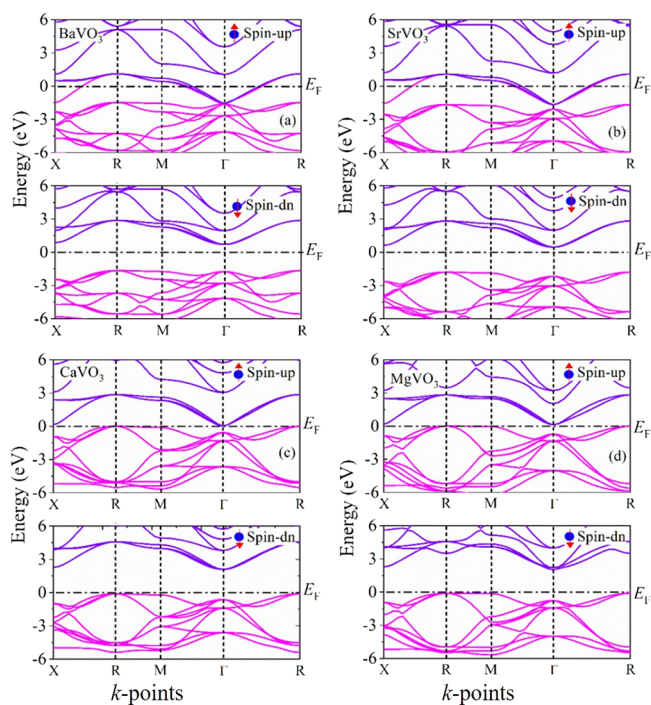
Figure 5. (Color online) Spin-polarized GGA+U (U = 2.5 eV for V 3d) calculated electronic band structures of (a) BaVO$_3$, (b) SrVO$_3$, (c) CaVO$_3$, and (d) MgVO$_3$ along the high-symmetry directions in the Brillouin zone.

SrVO$_3$, respectively, whereas in the case of CaVO$_3$ and MgVO$_3$, the band is a major contribution of O 2s with minor contributions of p and d states of V. Finally, the TDOS from −8 eV to the Fermi level (E_F) has primary contributions from V 3d and O 2p states along with minor contributions of the p state of V and d and s states of Ba and Sr atoms (Figure 6).

To clarify the physical origin of half-metallic ferromagnetism of AVO$_3$ compounds, we also studied the TDOS and PDOS at the E_F for the spin-up channel, which is shown in Figure 7. It is
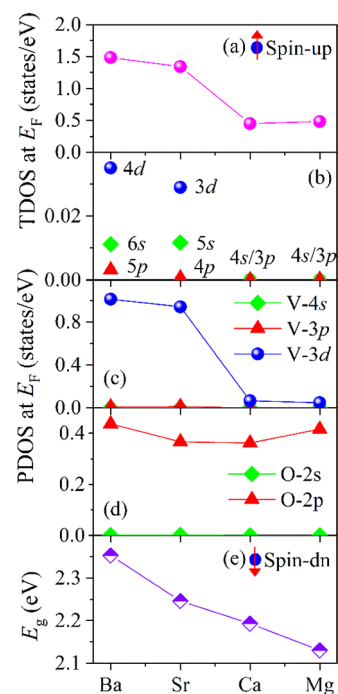
Figure 7. (Color online) (a−d) Total density of states (TDOS) and partial density of states (PDOS) at the Fermi level (E_F) of AVO$_3$. (e) Band gap energy (E_g) of AVO$_3$ in the spin-down channel.

higher energy with the alteration of the cation from Ba to Mg. The bands at about −25, −34, −42, and −39 eV of BaVO$_3$, SrVO$_3$, CaVO$_3$, and MgVO$_3$ come from the Ba 6s, Sr 5s, Ca 4s, and Mg 2p states, respectively. The band at around −18 eV of BaVO$_3$ and SrVO$_3$ is due to the admixture of dominating O 2s along with minor contributions of V 3p and 3d, Ba 5p and 4d, and Sr 4p and 3d states, whereas the band of CaVO$_3$ is due to the primary contribution of the Ca 3p state along with a little contribution of O 2s. Over these states, around −16 to −11 eV is demonstrated to be completely p states of Ba and Sr with the minor contributions of s and p states of O for BaVO$_3$ and
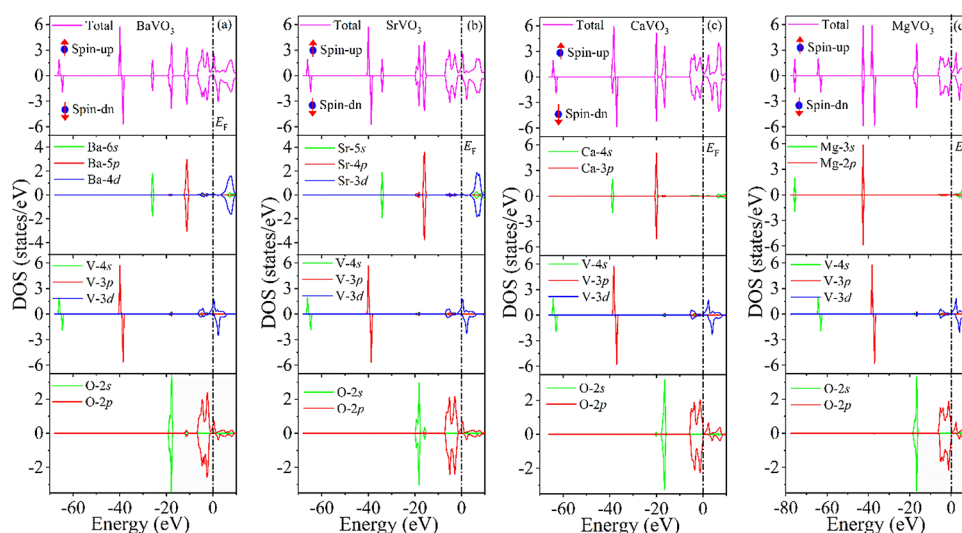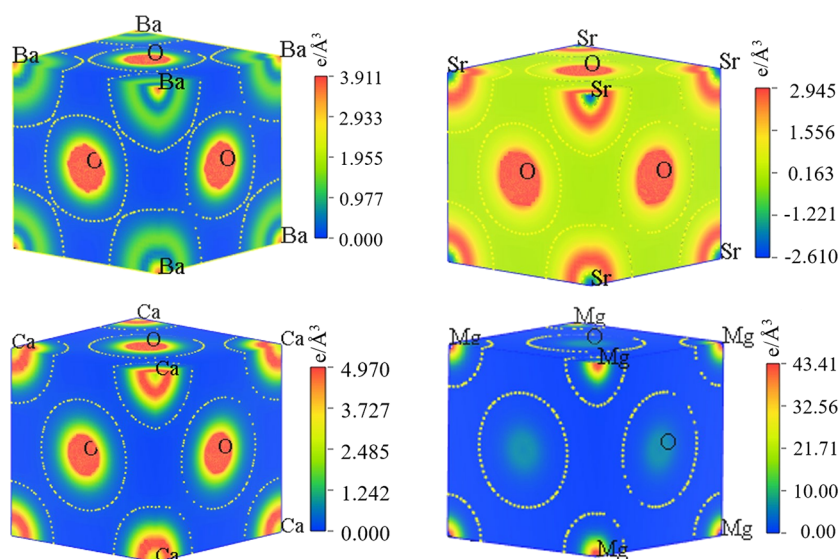
found from Figure 7 that the PDOS value of V 3d and O 2p states decreases by changing cations from Ba to Ca, and the PDOS value of V 3d becomes very small in CaVO$_3$ and

Figure 6. (Color online) Total and partial density of states of (a) BaVO$_3$, (b) SrVO$_3$, (c) CaVO$_3$, and (d) MgVO$_3$ with the spin-polarized GGA+U (U = 2.5 eV for V 3d) method.

Figure 8. (Color online) Electronic charge density of (upper left) BaVO$_3$, (upper right) SrVO$_3$, (lower left) CaVO$_3$, and (lower right) MgVO$_3$.
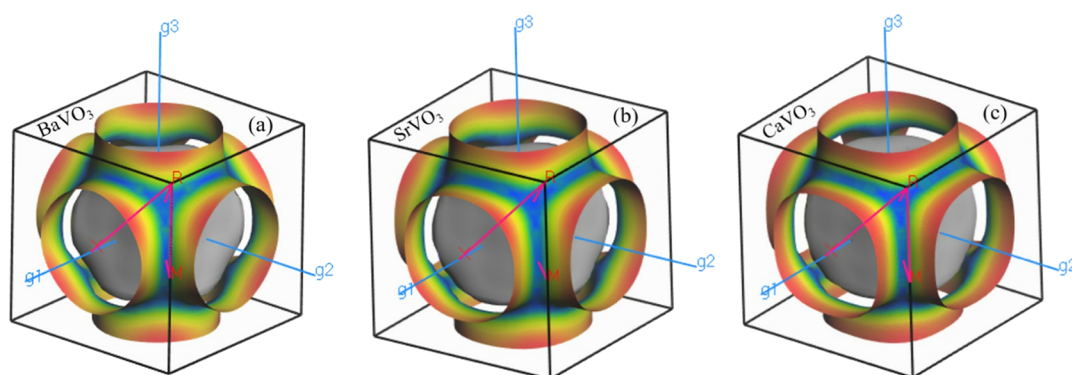
Figure 9. (Color online) Fermi surface topology of (a) BaVO$_3$, (b) SrVO$_3$, and (c) CaVO$_3$.

MgVO$_3$, while the PDOS value of the O 2p state increases in MgVO$_3$. These results indicate that the strong hybridization between V 3d and O 2p is responsible for the half-metallic and semiconductor nature of AVO$_3$, where the V 3d state controls the half-metallic behavior and O 2p dominates the semiconductor nature of the studied compounds.

3.3.3. Electronic Charge Density. The charge density maps of valence electrons are depicted in Figure 8 to comprehend the total electronic charge density distribution of AVO$_3$ compounds. The scale on the right side shows the intensity of electron density. The red color denotes the high density of electrons, whereas the blue color represents the low density of electrons. It is apparent from Figure 8 that the distribution of charge density is essentially spherical around all the atoms of AVO$_3$ compounds. This outcome indicates the ionic nature of AVO$_3$ compounds. The ionic characteristics are also an effect of the metallic characteristics of compounds. As can be seen in Figure 4b, the O−V bonds where the electronic charge transfer from V 3d to O 2p in AVO$_3$ (A = Ba, Ca, and Mg) manifest a half-metallic nature.

3.3.4. Fermi Surface. The Fermi surface topologies of AVO$_3$ compounds are shown in Figure 9. The Fermi surfaces of BaVO$_3$, SrVO$_3$, CaVO$_3$, and other compounds are almost similar. It is seen from the topology that there is a hole-like Fermi surface that looks like a cylindrical cross section with six windows surrounded at the Γ-point. A hole pocket is also

present around the X-point connected with the hole-like Fermi surface surrounding the Γ-point. Hence, it is evident that only hole-like Fermi surfaces are present, which reveals the single-band nature of AVO$_3$ (A = Ba, Sr, and Ca) compounds. However, the MgVO$_3$ compound does not show the Fermi surface topology for its semiconducting nature.

3.4. Optical Properties. The material's response to incident electromagnetic radiation can be explained by various optical properties, namely, the dielectric function, the refractive index, conductivity, the absorption coefficient, reflectivity, and the loss function. The real (ε_1) and imaginary (ε_2) parts of the dielectric function of AVO$_3$ compounds are displayed in Figure 10. The damping factor of 0.05 eV and the Drude plasma frequency of 3 eV have been used to study dielectric properties because of the half-metallic nature of AVO$_3$ in the present investigation. In this study, the position of the peak of the real part of the dielectric function is linked to the electron excitation, and the peak is primarily caused by interband transitions. It is apparent from Figure 10 that $\varepsilon_1(\omega)$ shows a peak in the visible region at around 2.30 eV, which is related to the interband transitions. It is well-known that the real part of the dielectric function is dominated by intraband trans-formations from the conduction electrons primarily in the low-energy infrared region for metallic systems. However, the real part of the dielectric function gives rise to interband transitions because of the half-metallic or semiconductor
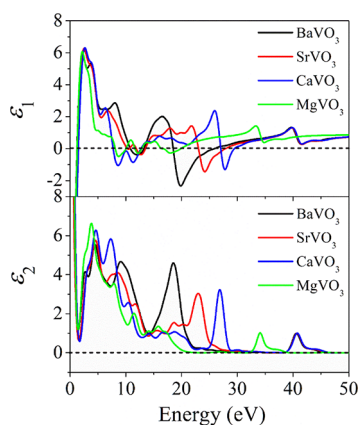
Figure 10. (Color online) Energy-dependent dielectric function (real part, ε_1, and imaginary part, ε_2) of AVO$_3$ compounds.

nature of AVO$_3$ in this study. The half-metallic behavior of AVO$_3$ (A = Ba, Sr, and Ca) compounds and semiconductor behavior of MgVO$_3$ are revealed on the basis of their electronic properties. It is important to note that $\varepsilon_2(\omega)$ reaches zero in the ultraviolet region at around 30 eV, which demonstrates that the AVO$_3$ compounds are transparent and optically anisotropic as well. The anisotropic behavior of AVO$_3$ compounds was also found by the elastic properties.

The extinction coefficient (k) and the refractive index (n) represent the amount of the absorption loss and the phase velocity, respectively, when the electromagnetic wave (as light) passes through the material. The energy-dependent n and k are shown in Figure 11. The calculated values of the static
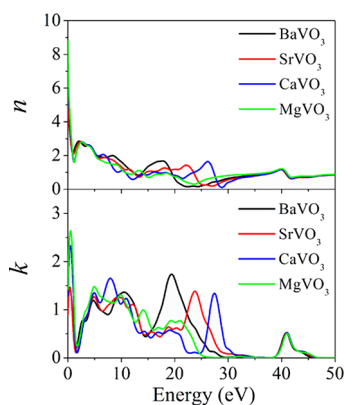
Figure 11. (Color online) Refractive index (n) and extinction coefficient (k) of AVO$_3$ compounds as a function of energy.

refractive index $n(0)$ of BaVO$_3$, SrVO$_3$, CaVO$_3$, and MgVO$_3$ are found to be 6.14, 5.97, 7.89, and 8.77, respectively, which changes with the applied energy, implying that AVO$_3$ carries photorefractive effects. The relatively high value of the static refractive index suggests that AVO$_3$ can be suited as a potential candidate for application as an ultrahigh-density optical storage device upon suitable laser irradiation.[59]

The coefficient of absorption (α) provides the measure of energy absorbed by materials and gives information about the solar energy conversion efficiency.[60] From the lower part of Figure 12, the spectra of the absorption coefficient start with a zero value, and the calculated α illustrates a trend similar to $\varepsilon_2(\omega)$. Generally, the peaks with the energy in the infrared range of spectra may arise due to the intraband transition. In
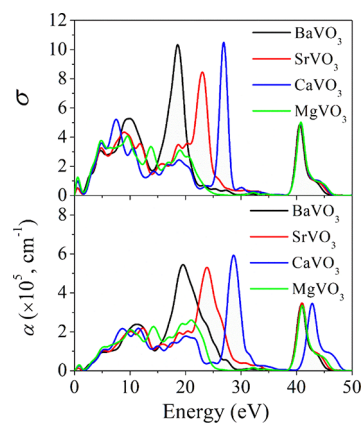

Figure 12. (Color online) Real parts of conductivity (σ) and absorption coefficient (α) of AVO$_3$ compounds as a function of energy.

contrast, the peaks in the high-energy region of the conductivity and absorption spectra may be from the interband transition. The maximum absorption is found at 19.54, 23.85, 27.47, and 41.02 eV for BaVO$_3$, SrVO$_3$, CaVO$_3$, and MgVO$_3$, respectively. The different high-intensity peaks in the range of 15−30 eV denote various electronic transition rates.

It is worth noting that the real part of the photoconductivity (σ) spectra of AVO$_3$ (upper part of Figure 12) begins with zero photon energy, albeit MgVO$_3$ shows a small band gap (E_g of ~0.12 eV) in the electronic band structure (Figure 5). Therefore, the conductivity at zero photon energy is a clear indication of the half-metallic nature of BaVO$_3$ and SrVO$_3$ compounds, whereas the conductivity at zero photon energy of MgVO$_3$ denotes the degenerate-like semiconductor material. Hence, the cubic phase of MgVO$_3$ can be a suitable candidate for photovoltaic applications. The maximum values of photoconductivity are observed at 18.62, 23.02, 26.87, and 40.46 eV for BaVO$_3$, SrVO$_3$, CaVO$_3$, and MgVO$_3$, respectively. It is noted from Figure 12 that the photoconductivity spectra vary with the absorption spectra. As a result of absorbing photons, the photoconductivity of AVO$_3$ increases, according to this finding.[61]

The energy-dependent reflectivity (R) spectra of AVO$_3$ are depicted in the upper part of Figure 13. The highest reflectivity of AVO$_3$ (A = Ba, Sr, and Ca) is seen in the ultraviolet region, while the highest reflectivity is found in the infrared region in
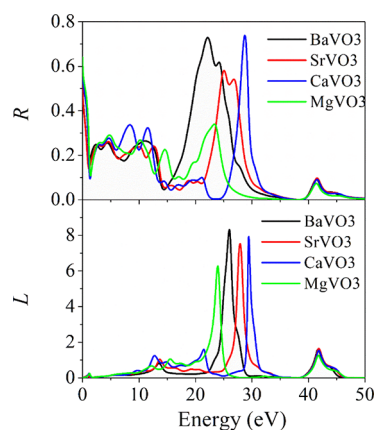
Figure 13. (Color online) Energy-dependent reflectivity (R) and loss function (L) of the AVO$_3$ compounds.

Table 5. Mulliken Atomic Population Analysis of AVO$_3$ Compounds

compounds	species	Mulliken atomic population						net magnetic moment (μ_B)
		s	p	d	total	charge (e)	spin (hbar/2)	
BaVO$_3$	Ba	2.00	5.97	0.76	8.73	1.27	−0.03	
	V	2.32	6.68	3.24	12.24	0.76	1.41	0.99
	O	1.84	4.84	0.00	6.68	−0.68	−0.13	
SrVO$_3$	Sr	2.02	5.99	0.66	8.67	1.33	−0.03	
	V	2.31	6.69	3.26	12.27	0.73	1.31	1.01
	O	1.83	4.86	0.00	6.69	−0.69	−0.09	
CaVO$_3$	Ca	2.04	5.99	0.53	8.57	1.43	−0.02	
	V	2.30	6.73	3.28	12.31	0.69	1.26	1.00
	O	1.83	4.88	0.00	6.71	−0.71	−0.08	
MgVO$_3$	Mg	2.30	6.36	0.00	8.65	1.35	−0.02	
	V	2.30	6.66	3.28	12.24	0.76	1.25	0.99
	O	1.82	4.88	0.00	6.70	−0.70	−0.08	

MgVO$_3$. The peaks in the ultraviolet region give rise to the interband transition, whereas the peaks in the infrared region stem from the intraband transition. The zero frequency value of reflectivity $R(0)$ is found to be 0.53, 0.52, 0.61, and 0.64 for BaVO$_3$, SrVO$_3$, CaVO$_3$, and MgVO$_3$, respectively. It is noted that the maximum reflectivity value at zero frequency is seen in the MgVO$_3$ compound. The high-reflectivity spectra of AVO$_3$ reflect that these materials can be a potential candidate for coating materials to diminish solar heating.

The loss spectra (L) of AVO$_3$ as a function of energy are shown in the lower part of Figure 13. The energy loss function denotes the loss of energy of a fast electron when it passes through a material.[62] The maximum loss function is connected to the plasma resonance, and the frequency associated with it is defined as the plasma frequency, ω_p.[63] The maximum loss function of BaVO$_3$, SrVO$_3$, CaVO$_3$, and MgVO$_3$ is found at 25.99, 27.91, 29.45, and 23.95 eV, respectively, which implies the plasma frequency of the respective compound. The results are similar to those observed in ATiO$_3$ (A = Ba, Sr, Ca, and Pb).[23] The AVO$_3$ materials become transparent when the incident light frequency is higher than the plasma frequency. In addition, the loss function peak related to ω_p corresponds to the zero-crossing of ε_1 with small ε_2 (Figure 10), and it correlates with the edge in the reflectivity spectrum in which a sudden reduction of the maximum reflectivity spectrum occurs (Figure 13). It is worth seeing that the value of ω_p increased by varying cations from Ba to Ca, while the value of ω_p significantly decreased in MgVO$_3$. The significant decrease in ω_p may be due to the semiconductor nature and/or the larger effective mass of free electrons of the MgVO$_3$ compound.

3.5. Population Analysis. The analysis of the Mulliken atomic population provides interesting information regarding the chemical bonding nature of solids.[64] The calculated Mulliken atomic populations of AVO$_3$ are listed in Table 4 gradually. As can be seen from Table 5, A (= Ba, Sr, Ca, and Mg) and V atoms carry positive charges, while O atoms carry negative charges, implying that the sharing of charges occurs from A and V to O atoms. We also studied the bond overlap population (P^μ) in order to have a better understanding of the bonding nature of the AVO$_3$ compounds. The zero value of the bond overlap population expresses a perfectly ionic bond, whereas the deviation from zero reflects the increasing levels of covalency.[65] The deviation of P^μ from zero is clearly seen in Table 6, which reveals the covalent nature of these compounds. It is noted in Table 6 that the V−O bond in BaVO$_3$ is more covalent than the other compounds. It is also

Table 6. The Calculated Mulliken Bond Number (n^μ), Bond Length (d^μ), and Bond Overlap Population (P^μ) of the AVO$_3$ Compounds

compounds	bonds	n^μ	d^μ (Å)	P^μ
BaVO$_3$	V−O	3	1.96337	0.92
	Ba−V	1	3.40065	−0.70
	O−O	3	2.77662	−0.13
SrVO$_3$	V−O	3	1.91503	0.88
	Sr−V	1	3.31693	−0.52
	O−O	3	2.70826	−0.15
CaVO$_3$	V−O	3	1.88698	0.87
	Ca−V	1	3.26835	−0.36
	O−O	3	2.66860	−0.17
MgVO$_3$	V−O	3	1.86655	0.85
	Mg−V	1	3.23296	−0.34
	O−O	3	2.63970	−0.20

found that the value of P^μ for the V−O bond is positive, whereas the value of P^μ is negative for the A−V (A = Ba, Sr, Ca, and Mg) and O−O bonds. The positive and negative magnitudes of P^μ denote the direct and indirect bonds of atoms involved in AVO$_3$ compounds, respectively. The calculated values of spin (Table 5) indicate that the V atom is mainly accountable for the magnetic properties of AVO$_3$ compounds. We have also calculated the net magnetic moments of AVO$_3$ and summarized them in Table 5. The detailed magnetic properties of AVO$_3$ compounds were studied by researchers earlier.[29] The net magnetic moments of AVO$_3$ under this inspection somewhat differ from the value reported in ref 29. However, the value of the net magnetic moment of BaVO$_3$ is in good agreement with the value found in ref 66.

3.6. Thermodynamic Properties. To understand the behavior of AVO$_3$ under high temperatures and pressures, we have investigated the various thermodynamic properties such as melting temperature, T_m, Debye temperature, θ_D, and minimum thermal conductivity, K_{min}. θ_D is an essential parameter of solids to rationalize some interesting physical processes related to phonons, specific heat, melting point, thermal conductivity, etc.[67] The value of θ_D can be estimated using the average sound velocity using the following equation:[67]

$$\theta_D = \frac{h}{k_B}\left[\frac{3m}{4\pi}\left(\frac{N_A\rho}{M}\right)\right]^{1/3}v_m \qquad (4)$$

Table 7. The Calculated Density, (ρ), Debye Temperature, (θ_D), Longitudinal, Transverse, and Average Sound Velocities (v_l, v_t, and v_m), Minimum Thermal Conductivity (K_{min}), and Melting Temperature (T_m) of AVO$_3$ Compounds

compounds	ρ (g/cm^3)	v_l (km/s)	v_t (km/s)	v_m (km/s)	θ_D (K)	T_m (K)	K_{min} (W m^{-1} K^{-1})	γ
BaVO$_3$	6.479	7140	4213	4668	605	1704	1.22	1.42
SrVO$_3$	5.514	7856	4567	5067	673	1861	1.39	1.47
CaVO$_3$	4.295	8810	4968	5526	745	1933	1.57	1.59
MgVO$_3$	3.909	8712	4351	4881	664	1906	1.41	2.01

where k_B and h denote the Boltzmann and Planck constants, respectively. ρ is the density, and N_A is Avogadro's number. V, m, and M are the volume of a unit cell, the number of atoms within a unit cell, and molecular weight, respectively. v_m implies the average sound velocity in the crystal, which is calculated using the following equation:

$$v_m = \left[\frac{1}{3}\left(\frac{2}{v_t^3} + \frac{1}{v_l^3}\right)\right]^{-1/3} \tag{5}$$

Here, v_t and v_l denote the transverse and longitudinal sound velocities, respectively. The following expressions can be used to calculate v_l and v_t using the shear modulus, G, and the bulk modulus, B:

$$v_l = \left(\frac{B + \frac{4}{3}G}{\rho}\right)^{1/2} \text{ and } v_t = [G/\rho]^{1/2} \tag{6}$$

The melting temperature, T_m, of the AVO$_3$ compounds has also been calculated via the following empirical formula using elastic constants, C_{ij}:[68]

$$T_m = 354 + \frac{4.5(2C_{11} + C_{33})}{3} \tag{7}$$

In a cubic structure, the axial lengths are equal; thus, C_{11}, C_{22}, and C_{33} are also equal.

Moreover, we calculated another important entity, that is, thermal conductivity, which is used to study the heat conduction of a material. It is well-established that the minimum thermal conductivity is directly concerned with the temperature. The temperature of a material gradually increases the conductivity of the material and, after that, gradually decreases to a certain value.[69]

Albeit many similar equations are available to predict the minimum thermal conductivity, in this report, the minimum thermal conductivity, K_{min} has been calculated by using the Clarke expression[70] and can be defined as follows:

$$K_{min} = k_B v_m (M/n\rho N_A)^{-2/3} \tag{8}$$

where k_B is the Boltzmann constant, v_m is the average sound velocity, M is the molecular mass, n is the number of atoms per molecule, and N_A is Avogadro's number used for the calculation.

The Grüneisen parameter (γ) provides information regarding anharmonic effects, i.e., the temperature-dependent phonon dampings and frequencies as well as the thermal expansion effects. The Grüneisen parameter is explained by the following:

$$\gamma(\omega_n) = \frac{d\ln(\omega_n)}{d(\ln(\Phi))} \tag{9}$$

where ω_n and Φ are the angular frequency and the packing fraction of crystals, respectively.[71] The value of γ can be

estimated by a simple expression related to Poisson's ratio[71] as follows:

$$\gamma = \frac{3(1 + \nu)}{2(2 - 3\nu)} \tag{10}$$

The calculated values of Debye temperature, θ_D, along with different sound velocities (v_l, v_t, and v_m), melting temperature, T_m, the Grüneisen parameter, γ, and minimum thermal conductivity, K_{min}, of AVO$_3$ under this study are listed in Table 7. In general, a higher Debye temperature is associated with a higher phonon thermal conductivity and vice-versa. The relatively high values of θ_D and K_{min} of AVO$_3$ imply high thermal conductivity, and they might not be suitable for use as thermal barrier coating (TBC) materials.

4. CONCLUSIONS

In this study, we have investigated various physical properties of the cubic phase of AVO$_3$ (A = Ba, Sr, Ca, and Mg) compounds. The calculated lattice parameters show very fair agreement with the available experimental data, implying the reliability of these computational calculations. The mechanical stability of AVO$_3$ is confirmed by the Born stability criteria. The Poisson's and Pugh's ratios reveal the ductile behavior of CaVO$_3$ and MgVO$_3$, whereas a brittle nature is exhibited by BaVO$_3$ and SrVO$_3$. The analysis of various anisotropy indices shows that BaVO$_3$, CaVO$_3$, and MgVO$_3$ are anisotropic, whereas SrVO$_3$ exhibits insignificant anisotropy. The intermediate values of Peierls stress were found in AVO$_3$. The AVO$_3$ (A = Ba, Sr) compounds exhibit half-metallic character, whereas CaVO$_3$ and MgVO$_3$ show spin-glass and magnetic semiconductor-like behavior alongwith n-type carriers, respectively. The half-metallic nature of AVO$_3$ stems mainly from p−d hybridization between O and V atoms. The single-band nature and the presence of hole-like Fermi surfaces are seen. The bonding properties reveal that AVO$_3$ possesses intra-atomic bonding with a mixture of covalent, ionic, and metallic interactions. Numerous thermodynamic behaviors of AVO$_3$ are calculated using relevant equations and analyzed properly based on the obtained results. The study of optical properties, especially the refractive index of these compounds, indicates that all the materials could be used as promising high-density optical data storage.

■ AUTHOR INFORMATION

Corresponding Authors

Md. Mijanur Rahaman − *Department of Materials Science and Engineering, University of Rajshahi, Rajshahi 6205, Bangladesh;* ● orcid.org/0000-0002-8877-6465; Email: mijan_mse@ru.ac.bd

Mirza Humaun Kabir Rubel − *Department of Materials Science and Engineering, University of Rajshahi, Rajshahi 6205, Bangladesh;* ● orcid.org/0000-0001-9420-4335; Email: mhk_mse@ru.ac.bd

Authors

Khandaker Monower Hossain − *Department of Materials Science and Engineering, University of Rajshahi, Rajshahi 6205, Bangladesh*

A. K. M. Azharul Islam − *Department of Physics, University of Rajshahi, Rajshahi 6205, Bangladesh; International Islamic University Chittagong, Chittagong 4318, Bangladesh*

Seiji Kojima − *Graduate School of Pure and Applied Sciences, University of Tsukuba, Tsukuba, Ibaraki 305-8573, Japan;* ⊙ orcid.org/0000-0003-1933-9269

Complete contact information is available at:
https://pubs.acs.org/10.1021/acsomega.2c01630

Notes

The authors declare no competing financial interest.

■ REFERENCES

(1) Rahaman, M. M.; Imai, T.; Sakamoto, T.; Tsukada, S.; Kojima, S. Fano resonance of Li-doped $KTa_{1−x}Nb_xO_3$ single crystals studied by Raman scattering. *Sci. Rep.* **2016**, *6*, 23898.

(2) Rubel, M. H. K.; Takei, T.; Kumada, N.; Ali, M. M.; Miura, A.; Tadanaga, K.; Oka, K.; Azuma, M.; Magome, E.; Moriyoshi, C.; Kuroiwa, Y. Hydrothermal synthesis, structure, and superconductivity of simple cubic perovskite $(Ba_{0.62}K_{0.38})(Bi_{0.92}Mg_{0.08})O_3$ with $Tc \sim 30$ K. *Inorg. Chem.* **2017**, *56*, 3174−3181.

(3) Rubel, M. H. K.; Ali, M. M.; Ali, M. S.; Parvin, R.; Rahaman, M. M.; Hossain, K. M.; Hossain, M. I.; Islam, A. K. M. A.; Kumada, N. First−principles study: Structural, mechanical, electronic and thermodynamic properties of simple-cubic-perovskite $(Ba_{0.62}K_{0.38})$-$(Bi_{0.92}Mg_{0.08})O_3$. *Solid State Commun.* **2019**, *288*, 22−27.

(4) Wei, Y.; Gui, H.; Zhao, Z.; Li, J.; Liu, Y.; Xin, S.; Li, X.; Xie, W. Structure and magnetic properties of the perovskite $YCo_{0.5}Fe_{0.5}O_3$. *AIP Adv.* **2014**, *4*, 127134.

(5) Pradhan, D. K.; Mohanty, H. S.; Kumari, S.; Bhoi, K.; Tang, N.; Ravikant; Rahaman, M. M.; Pradhan, D. K.; Kumar, A.; Gilbertah, D. A.; Rack, P. D. Ferroic phase transitions and magnetoelectric coupling in cobalt doped $BaTiO_3$. *J. Mater. Chem. C* **2021**, *9*, 12694−12711.

(6) Varignon, J.; Bristowe, N. C.; Bousquet, E.; Ghosez, P. Coupling and electrical control of structural, orbital and magnetic orders in perovskites. *Sci. Rep.* **2015**, *5*, 15364.

(7) Blake, G. R.; Palstra, T. T. M.; Ren, Y.; Nugroho, A. A.; Menovsky, A. A. Transition between Orbital Orderings in YVO_3. *Phys. Rev. Lett.* **2001**, *87*, No. 245501.

(8) Mossanek, R. J. O.; Abbate, M.; Fonseca, P. T.; Fujimori, A.; Eisaki, H.; Uchida, S.; Tokura, Y. Optical conductivity and x-ray absorption spectra of the Mott-Hubbard compounds RVO_3 (R=Sr, Ca, La, and Y). *Phys. Rev. B* **2009**, *80*, 195107.

(9) Uratani, Y.; Shishidou, T.; Ishii, F.; Oguchi, T. First-Principles Predictions of Giant Electric Polarization. *Jpn. J. Appl. Phys.* **2005**, *44*, 7130.

(10) Okos, A.; Colin, C.; Darie, C.; Raita, O.; Bordet, P.; Pop, A. Structure and magnetic properties of the layered perovskite $PbVO_3$. *J. Alloys Compd.* **2014**, *602*, 265−268.

(11) Belik, A. A.; Azuma, M.; Saito, T.; Shimakawa, Y.; Takano, M. Crystallographic features and tetragonal phase stability of $PbVO_3$, a new member of $PbTiO_3$ family. *Chem. Mater.* **2005**, *17*, 269−273.

(12) Nishimura, K.; Yamada, I.; Oka, K.; Shimakawa, Y.; Azuma, M. High-pressure synthesis of $BaVO_3$: A new cubic perovskite. *J. Phys. Chem. Solids* **2014**, *75*, 710−712.

(13) Lan, Y. C.; Chen, X. L.; He, M. Structure, magnetic susceptibility and resistivity properties of $SrVO_3$. *J. Alloys Compd.* **2003**, *354*, 95−98.

(14) Ueda, Y. Oxygen nonstoichiometry, structures, and physical properties of $CaVO_{3−δ}$: I. A series of new oxygen-deficient phases. *J. Solid State Chem.* **1998**, *135*, 36−42.

(15) Bouloux, J.-C.; Milosevic, I.; Galy, J. Les hypovanadates de magnésium $MgVO_3$ et MgV_2O_5. Structure cristalline de $MgVO_3$. *J. Solid State Chem.* **1976**, *16*, 393−398.

(16) Zhang, L.; Zhou, Y.; Guo, L.; Zhao, W.; Barnes, A.; Zhang, H. T.; Eaton, C.; Zheng, Y.; Brahlek, M.; Haneef, H. F.; Podraza, N. J.; Chan, M. H. W.; Gopalan, V.; Rabe, K. M.; Engel-Herbert, R. Correlated metals as transparent conductors. *Nat. Mater.* **2016**, *15*, 204−210.

(17) Falcón, H.; Alonso, J. A.; Casais, M. T.; Martínez-Lope, M. J.; Sánchez-Benítez, J. Neutron diffraction study, magnetism and magnetotransport of stoichiometric $CaVO_3$ perovskite with positive magnetoresistance. *J. Solid State Chem.* **2004**, *177*, 3099−3104.

(18) Chamberland, B. L.; Danielson, P. S. Alkaline-earth vanadium (IV) oxides having the AVO_3 composition. *J. Solid State Chem.* **1971**, *3*, 243−247.

(19) Giannakopoulou, V.; Odier, P.; Bassat, J. M.; Loup, J. P. $SrVO_3$ and Sr_2VO_4, electrical properties below and above room T. *Solid State Commun.* **1995**, *93*, 579−583.

(20) Shirakawa, N.; Murata, K.; Makino, H.; Iga, F.; Nishihara, Y. Scaling of negative magnetoresistance and extraordinary Hall Effect in $CaVO_{3-δ}$. *J. Phys. Soc. Jpn.* **1995**, *64*, 4824−4833.

(21) Inoue, I. H.; Morikawa, K.; Fukuchi, H.; Tsujii, T.; Iga, F.; Nishihara, Y. Metal-to-insulator transitions in CaVOy. *Phys. B* **1994**, *194-196*, 1067−1068.

(22) Chamberland, B. L.; Danielson, P. S.; Moeller, C. W. A high-pressure modification of $MgVO_3$. *J. Solid State Chem.* **1978**, *26*, 377−382.

(23) Chaplygin, I.; Hayn, R.; Koepernik, K. Electronic structure of the spin-1/2 chain compound $MgVO_3$. *Phys. Rev. B* **1999**, *60*, R12557−R12560.

(24) Kamruzzaman, M.; Helal, M. A.; Ara, I. E.; Farid Ul Islam, A. K. M.; Rahaman, M. M. A comparative study based on the first principles calculations of $ATiO_3$ (A = Ba, Ca, Pb and Sr) perovskite structure. *Indian J. Phys.* **2016**, *90*, 1105−1113.

(25) Rubel, M. H. K.; Mitro, S. K.; Mondal, B. K.; Rahaman, M. M.; Saiduzzaman, M.; Hossain, J.; Islam, A. K. M. A.; Kumada, N. Newly synthesized A-site ordered cubic-perovskite superconductor $(Ba_{0.54}K_{0.46})_4Bi_4O_{12}$: A DFT investigation. *Phys. C* **2020**, *574*, 1353669.

(26) Rubel, M. H. K.; Hadi, M. A.; Rahaman, M. M.; Ali, M. S.; Aftabuzzaman, M.; Parvin, R.; Islam, A. K. M. A.; Kumada, N. Density functional theory study of a new Bi-based $(K_{1.00})$-$(Ba_{1.00})_3(Bi_{0.89}Na_{0.11})_4O_{12}$ double perovskite superconductor. *Comput. Mater. Sci.* **2017**, *138*, 160−165.

(27) Hauge, H. I. T.; Verheijen, M. A.; Conesa-Boj, S.; Etzelstorfer, T.; Watzinger, M.; Kriegner, D.; Zardo, I.; Fasolato, C.; Capitani, F.; Postorino, P.; Kölling, S.; Li, A.; Assali, S.; Stangl, J.; Bakkers, E. P. A. M. Hexagonal silicon realized. *Nano Lett.* **2015**, *15*, 5855−5860.

(28) Rashid, M.; Abbas, Z.; Yaseen, M.; Afzal, Q.; Mahmood, A.; Ramay, S. M. Theoretical investigation of cubic $BaVO_3$ and $LaVO_3$ perovskites via Tran−Blaha-Modified Becke−Johnson exchange potential approach. *J. Supercond. Novel Magn.* **2017**, *30*, 3129−3136.

(29) Mahmood, Q.; Ali, S. A.; Hassan, M.; Laref, A. First principles study of ferromagnetism, optical and thermoelectric behaviours of AVO_3 (A = Ca, Sr, Ba) perovskites. *Mater. Chem. Phys.* **2018**, *211*, 428−437.

(30) Hohenberg, P.; Kohn, W. Inhomogeneous electron gas. *Phys. Rev.* **1964**, *136*, B864−B871.

(31) Kohn, W.; Sham, L. J. Self-consistent equations including exchange and correlation effects. *Phys. Rev.* **1965**, *140*, A1133−A1138.

(32) Clark, S. J.; Segall, M. D.; Probert, M. J.; Pickard, C. J.; Hasnip, P. J.; Payne, M. C. First principles methods using CASTEP. *Z. Kristallogr.* **2005**, *220*, 567.

(33) Vanderbilt, D. Soft self-consistent pseudopotentials in a generalized eigenvalue formalism. *Phys. Rev. B* **1990**, *41*, 7892−7895.

(34) Head, J. D.; Zerner, M. C. A Broyden-fletcher-goldfarb-shanno optimization procedure for molecular geometries. *Chem. Phys. Lett.* **1985**, *122*, 264−270.

(35) Monkhorst, H. J.; Pack, J. D. Special points for Brillouin-zone integrations. *Phys. Rev. B* **1976**, *13*, 5188−5192.

(36) Rubel, M. H. K.; Hossain, K. M.; Mitro, S. K.; Rahaman, M. M.; Hadi, M. A.; Islam, A. K. M. A. Comprehensive first-principles calculations on physical properties of ScV_2Ga_4 and ZrV_2Ga_4 in comparison with superconducting HfV2Ga4. *Mater. Today Commun.* **2020**, *24*, 100935.

(37) Murnaghan, F. D. *Finite deformation of an elastic solid*; Wiley: New York, 1951.

(38) Born, M. Thermodynamics of crystals and melting. *J. Chem. Phys.* **1939**, *7*, 591−603.

(39) Jamal, M.; Asadabadi, S. J.; Ahmad, I.; Aliabad, H. A. R. Elastic constants of cubic crystals. *Comput. Mater. Sci.* **2014**, *95*, 592−599.

(40) Kleinman, L. Deformation potentials in silicon. I. Uniaxial strain. *Phys. Rev.* **1962**, *128*, 2614−2621.

(41) Elias, B. H.; Ilyas, B. M.; Saadi, N. S. A first principle study of the perovskite lanthanum Aluminate. *Mater. Res. Express* **2018**, *5*, 086302.

(42) Hill, R. The elastic behaviour of a crystalline aggregate. *Proc. Phys. Soc., A* **1952**, *65*, 349−354.

(43) Bouhemadou, A. First-principles study of structural, electronic and elastic properties of Nb_4AlC_3. *Braz. J. Phys.* **2010**, *40*, 52−57.

(44) Maradudin, A. A.; Montroll, E. W.; Weiss, G. H.; Ipatova, I. P. *Theory of lattice dynamics in the harmonic approximation*; Academic Press: New York, 1971.

(45) Nasir, M. T.; Hadi, M. A.; Rayhan, M. A.; Ali, M. A.; Hossain, M. M.; Roknuzzaman, M.; Naqib, S. H.; Islam, A. K. M. A.; Uddin, M. M.; Ostrikov, K. First-Principles Study of Superconducting ScRhP and ScIrP pnictides. *Phys. Status Solidi B* **2017**, *254*, 1700336.

(46) Wang, X.; Xiang, H.; Sum, X.; Liu, J.; Hou, F.; Zhou, Y. Mechanical properties and damage tolerance of bulk $Yb_3Al_5O_{12}$ ceramic. *J. Mater. Sci. Technol.* **2015**, *31*, 369−374.

(47) Rahaman, M. M.; Rubel, M. H. K.; Rashid, M. A.; Alam, M. A.; Hossain, K. M.; Hossain, M. I.; Khatun, A. A.; Hossain, M. M.; Islam, A. K. M. A.; Kojima, S.; Kumada, N. Mechanical, electronic, optical, and thermodynamic properties of orthorhombic $LiCuBiO_4$ crystal: a first-principles study. *J. Mater. Res. Technol.* **2019**, *8*, 3783−3794.

(48) Chen, X.-Q.; Niu, H.; Li, D.; Li, Y. Modeling hardness of polycrystalline materials and bulk metallic glasses. *Intermetallics* **2011**, *19*, 1275−1281.

(49) Mazhnik, E.; Oganov, A. R. A model of hardness and fracture toughness of solids. *J. Appl. Phys.* **2019**, *126*, 125109.

(50) Pugh, S. F. XCII. Relations between the elastic moduli and the plastic properties of polycrystalline pure metals. *Philos. Mag.* **1954**, *45*, 823−843.

(51) Frantsevich, I. N.; Voronov, F. F.; Bokuta, S. A. *Elastic constants and elastic moduli of metals and insulators*; Handbook, edited by Frantsevich, I. N. (Naukova Dumka: Kiev, (1983) pp.60−180.

(52) Pettifor, D. G. Theoretical predictions of structure and related properties of intermetallics. *Mater. Sci. Technol.* **1992**, *8*, 345−349.

(53) Wang, J. N. A new modification of the formulation of Peierls stress. *Acta Metall.* **1996**, *44*, 1541−1546.

(54) Ali, M. S.; Aftabuzzaman, M.; Roknuzzaman, M.; Rayhan, M. A.; Parvin, F.; Ali, M. M.; Rubel, M. H. K.; Islam, A. K. M. A. New superconductor $(Na_{0.25}K_{0.45})$ $Ba_3Bi_4O_{12}$: A first-principles study. *Phys. C* **2014**, *506*, 53−58.

(55) Hossain, M. A.; Ali, M. S.; Parvin, F.; Islam, A. K. M. A. Mechanical and optical properties of inverse-perovskites Sc_3InX (X = B, C, N). *Comput. Mater. Sci.* **2013**, *73*, 1−8.

(56) Music, D.; Schneider, J. M. Elastic properties of $Sr_{n+1}Ti_nO_{3n+1}$ phases (n = 1−3,∞). *J. Phys.: Condens. Matter* **2008**, *20*, No. 055224.

(57) Rubel, M. H. K.; Takei, T.; Kumada, N.; Ali, M. M.; Miura, A.; Tadanaga, K.; Oka, K.; Azuma, M.; Magomae, E.; Moriyoshi, C.; Kuroiwa, Y. Hydrothermal synthesis of a new Bi-based $(Ba_{0.82}K_{0.18})$-$(Bi_{0.53}Pb_{0.47})O_3$ superconductor. *J. Alloys Compd.* **2015**, *634*, 208−214.

(58) Yan, S.-Y.; Xie, Y.; Liu, T.; Yu, H.-T. Electronic structures and ferroelectric instabilities of cubic AVO_3 (A = Sr, Ba, and Pb) perovskites by first-principles calculations. *J. Phys.: Condens. Matter* **2010**, *22*, 125501.

(59) Rubel, M. H. K.; Islam, M. S.; Mahmuda, U. S. M.; Rahaman, M. M.; Hossain, M. E.; Parvez, M. S.; Hossain, K. M.; Hossain, M. I.; Hossain, J.; Yamanaka, J.; Kumada, N.; Kojima, S. $Ca_xBa_{1−x}Nb_2O_6$ ferroelectric nanopowders for ultrahigh-density optical data storage. *ACS Appl. Nano Mater.* **2018**, *1*, 6289−6300.

(60) Li, S.; Ahuja, R.; Barsoum, M. W.; Jena, P.; Johansson, B. Optical properties of Ti_3SiC_2 and Ti_4AlN_3. *Appl. Phys. Lett.* **2008**, *92*, 221907.

(61) Sun, J.; Zhou, X.-F.; Fan, Y.-X.; Chen, J.; Wang, H.-T.; Guo, X.; He, J.; Wang, Y. First-principles study of electronic structure and optical properties of heterodiamond BC_2N. *Phys. Rev. B* **2006**, *73*, 045108.

(62) Parvin, F.; Hossain, M. A.; Ali, M. S.; Islam, A. K. M. A. Mechanical, electronic, optical, thermodynamic properties and superconductivity of $ScGa_3$. *Phys. B* **2015**, *457*, 320−325.

(63) Fox, M. *Optical properties of solids*; Academic Press: New York, 1972.

(64) Mulliken, R. S. Electronic Population Analysis on LCAO−MO Molecular Wave Functions. I. *J. Chem. Phys.* **1955**, *23*, 1833−1840.

(65) Segall, M. D.; Shah, R.; Pickard, C. J.; Payne, M. C. Population analysis of plane-wave electronic structure calculations of bulk materials. *Phys. Rev. B* **1996**, *54*, 16317−16320.

(66) The Materials Project. *Materials Data on BaVO3 by Materials Project*; U.S. Department of Energy: United States N. p., 2020. Web. doi: DOI: 10.17188/1349744.

(67) Anderson, O. L. A simplified method for calculating the debye temperature from elastic Constants. *J. Phys. Chem. Solids* **1963**, *24*, 909−917.

(68) Fine, M. E.; Brown, L. D.; Marcus, H. L. Elastic constants versus melting temperature in metals. *Scr. Metall.* **1984**, *18*, 951−956.

(69) Shen, Y.; Clarke, D. R.; Fuierer, P. A. Anisotropic thermal conductivity of the Aurivillus phase, bismuth titanate ($Bi_4Ti_3O_{12}$): A natural nanostructured superlattice. *Appl. Phys. Lett.* **2008**, *93*, 102907.

(70) Clarke, D. R. Materials selection guidelines for low thermal conductivity thermal barrier coatings. *Surf. Coat. Technol.* **2003**, *163-164*, 67−74.

(71) Belomestnykh, V. N.; Tesleva, E. P. Interrelation between anharmonicity and lateral strain in quasiisotropic polycrystalline solids. *Tech. Phys.* **2004**, *49*, 1098−1100.